Supersonic Mass-Flux Measurements via Tunable Diode Laser Absorption and Nonuniform Flow Modeling

Leyen S. Chang,* Christopher L. Strand,† Jay B. Jeffries,‡ and Ronald K. Hanson§
Stanford University, Stanford, California 94305-3032
and
Glenn S. Diskin,¶ Richard L. Gaffney,** and Diego P. Capriotti††
NASA Langley Research Center, Hampton, Virginia 23681

Measurements of mass flux are obtained in a vitiated supersonic ground-test facility using a sensor based on line-of-sight diode laser absorption of water vapor. Mass flux is determined from the product of measured velocity and density. The relative Doppler shift of an absorption transition for beams directed upstream and downstream in the flow is used to measure velocity. Temperature is determined from the ratio of absorption signals of two transitions ($\lambda_1 = 1349$ nm and $\lambda_2 = 1341.5$ nm) and is coupled with a facility pressure measurement to obtain density. The sensor exploits wavelength-modulation spectroscopy with second-harmonic detection for large signal-to-noise ratios and normalization with the 1f signal for rejection of non-absorption-related transmission fluctuations. The sensor line of sight is translated both vertically and horizontally across the test section for spatially resolved measurements. Time-resolved measurements of mass flux are used to assess the stability of flow conditions produced by the facility. Measurements of mass flux are within 1.5% of the value obtained using a facility predictive code. The distortion of the wavelength-modulation spectroscopy lineshape caused by boundary layers along the laser line of sight is examined and the subsequent effect on the measured velocity is discussed. A method for correcting measured velocities for flow nonuniformities is introduced and application of this correction brings measured velocities within 4 m/s of the predicted value in a 1630 m/s flow.

Nomenclature

a	=	frequency-modulation depth, cm^{-1}
c	=	speed of light in vacuum, m/s
E''	=	lower state energy of absorption transition, cm^{-1}
f	=	modulation frequency, Hz
$\bar{I}_o$	=	average laser intensity
I_ν	=	spectral intensity, W/cm^2 s^{-1}
i_o	=	linear intensity modulation amplitude
k_ν	=	spectral absorption coefficient
L	=	path length, cm
m	=	modulation index
P	=	pressure, atm
S	=	linestrength, cm^{-2}/atm
T	=	temperature, K
U	=	velocity, m/s
x	=	spatial coordinate along line of sight, cm
α_ν	=	spectral absorbance
$\Delta\nu$	=	frequency shift, cm^{-1}
θ	=	crossing half-angle between two beams for Doppler shift measurement
ν	=	optical frequency, cm^{-1}
$\bar{\nu}$	=	average laser frequency, cm^{-1}
ν_o	=	transition linecenter frequency, cm^{-1}
ρ	=	density, kg/m^3
ϕ	=	lineshape function
ψ_1	=	linear intensity–frequency phase shift, rad

*Graduate Research Assistant, High Temperature Gasdynamics Laboratory, Department of Mechanical Engineering. Student Member AIAA.
†Graduate Research Assistant, High Temperature Gasdynamics Laboratory, Department of Mechanical Engineering.
‡Senior Research Associate, High Temperature Gasdynamics Laboratory, Department of Mechanical Engineering. Associate Fellow AIAA.
§Professor, High Temperature Gasdynamics Laboratory, Department of Mechanical Engineering. Fellow AIAA.
¶Senior Research Scientist, Chemistry and Dynamics Branch. Senior Member AIAA.
**Aerospace Engineer, Hypersonic Airbreathing Propulsion Branch. Senior Member AIAA.
††Research Engineer, Hypersonic Airbreathing Propulsion Branch.

I. Introduction

ACCURATE measurements of gas dynamic properties such as mass flux, temperature, and velocity are necessary for the characterization of ground-test facilities and for quantifying performance of advanced propulsion systems. In particular, mass flux is an important component in calculations of engine parameters such as thrust and specific impulse for airbreathing propulsion systems; in a supersonic combustion ramjet (scramjet) for example, a measurement of mass capture to within 1% uncertainty is necessary for a 1% uncertainty in the specific impulse [1]. Hence the development of accurate and robust sensors for the measurement of mass flux is critical for both in-flight and ground-testing of propulsion systems; this work focuses on the development of such a sensor for vitiated ground-test facilities, which are often used to reproduce hypersonic flight conditions, either by matching flight enthalpy or velocity. A common method for generating high-enthalpy flow is by combustion-heating the air, then expanding the flow through a supersonic nozzle with optional O_2 replenishment [2]. Conventional invasive mass-flux probes tend to disturb the flow and generate shock structures and may have limited ability to survive long-duration runs [3]. Noninvasive optical sensors are an ideal solution for testing in this type of environment; additionally, the high water mole fraction due to combustion allows for the use of widely available tunable diode lasers to access H_2O absorption transitions in the 1.4 μm range.

Tunable diode laser absorption spectroscopy (TDLAS) has been proven as a robust, noninvasive measurement technique for the harsh environments commonly experienced in high-speed or combusting propulsion flows. Mass-flux sensing via TDLAS was pioneered by

Philippe and Hanson [4] and patented for thrust measurements in 1993 [5]. Subsequent TDL mass-flux sensors have been deployed for a variety of field tests, including a commercial turbofan (PW6000) inlet at Pratt and Whitney [6], a full-scale Pratt & Whitney F-100 engine in an open ground-test stand at the NASA Dryden Flight Research Facility [7], and a model scramjet combustor at Wright-Patterson Air Force Base [3]. A TDLAS sensor employing wavelength-modulation spectroscopy (WMS) for measurement of mass flux using water vapor absorption was previously tested in a subsonic tunnel with uniform flow [8]. Optimization of this sensor for high-enthalpy flows is discussed here. The sensor was subsequently deployed in a combustion-heated supersonic ground-test facility [NASA Langley Direct-Connect Supersonic Combustion Test Facility (DCSCTF)] for spatially and temporally resolved mass-flux measurements in the tunnel isolator section. These results are compared with the facility predictive code and computational fluid dynamics (CFD) solutions to assess sensor accuracy and to examine the influence of the nonuniformities predicted by the CFD on the sensor-determined values.

TDLAS measurements are based upon Beer's law, where attenuation of the transmitted light is path-integrated along the line of sight. When temperature, pressure, and composition are uniform in the absorption path, the detected lineshape is a well-defined function of the gas properties. The ratio of two lineshapes provides a means to determine temperature, and velocity can be inferred from the Doppler shift of a lineshape. However, the lineshape can become distorted in the presence of nonuniform pressure, temperature, velocity, or gas composition. This distortion is a function of the degree of nonuniformity and the pressure and temperature dependence of the selected transition. Distortion of the lineshape can shift the apparent transition linecenter, producing an error in the measured Doppler shift. Spatially resolved CFD is used here to evaluate the effects of nonuniformity on a line-of-sight (LOS) measurement with an eventual goal of developing design rules to minimize the influence of nonuniformities. This analysis is used to adjust the TDLAS measurements to account for nonuniformity in the DCSCTF flow.

II. Simulation of Path-Integrated WMS Line Shapes from Nonuniform Flowfields

A. Theory

TDLAS is most accurate under conditions where the absorbing medium is uniform along the beam path. Gradients in velocity, temperature, pressure and composition, as well as physical obstructions and stagnant regions, can cause distortion to the detected lineshape. In this section, the equations describing the detected lineshape in a nonuniform absorbing medium will be developed.

As described in [8], the $1f$-normalized WMS-$2f$ signal (WMS-$2f/1f$) enables rejection of non-absorption-related transmission fluctuations and also improves velocity resolution. This sensor was demonstrated recently in a high-uniformity, low-speed tunnel to accurately measure velocities within 0.5 m/s of the facility set point [8]. In an earlier study, with an O_2 sensor, Lyle et al. [6] demonstrated that at low velocities, the distortion to the detected lineshape caused by boundary layers is nearly negligible. Knowing the fraction of the beam path passing through stagnant regions of absorption, a simple linear correction can be applied to remove the effects of the low-velocity regions [6,7]. This technique was demonstrated at subsonic velocities by simulations assuming simple step-function changes in velocity. However, at high velocities, the larger Doppler shift results in more noticeable distortion in the lineshape. Actual flows possess continuous gradients in velocity, temperature, pressure, and mole fraction that are poorly described by a step function. To accurately simulate lineshapes produced in nonuniform flows, we begin by considering the equation of radiative transfer in the case of absorption only:

$$\mathrm{d}I_\nu(x) = -k_\nu(x)I_\nu(x)\mathrm{d}x \tag{1}$$

Here, the spectral intensity I_ν and the spectral absorption coefficient k_ν depend on position in the absorbing medium, x. Next, we integrate

with respect to x and use the boundary condition $I_\nu(0) = I_{\nu,o}$ to obtain the transmitted intensity I_ν:

$$I_\nu = I_{\nu,o}\exp\left(\int_0^L -k_\nu\,\mathrm{d}x\right) = I_{\nu,o}\exp(-\alpha_\nu) \tag{2}$$

In the case of a uniform absorbing gas sample, Eq. (2) reduces to the familiar form of Beer's law. Instead, we retain the integral from 0 to L, the path length, recognizing that the spectral absorption coefficient may vary along the laser line of sight. The spectral absorbance, α_ν, introduced here will be examined in more detail below. The transmitted intensity along a nonuniform absorption path defined in Eq. (2) will be refined as the equations needed to simulate the WMS lineshape are developed.

A brief introduction to WMS theory is now given; nomenclature will follow [8–11]. The injection current of the diode laser is driven with a high-frequency sinusoid superimposed on a lower-frequency wavelength scan. Current modulation results in simultaneous modulation of laser frequency and intensity, and the instantaneous values are given by

$$\nu(t) = \bar{\nu} + a\cos(2\pi f t) \tag{3}$$

$$I_0(t) = \bar{I}_0 + i_0\cos(2\pi f t + \psi_1) \tag{4}$$

In Eq. (3), $\bar{\nu}(t)$ is the laser frequency (cm^{-1}) averaged over the modulation, f is the modulation frequency (Hz), and a is the modulation depth (cm^{-1}). In Eq. (4), $\bar{I}_0(t)$ is the laser intensity averaged over the modulation, i_0 is the linear intensity modulation amplitude, and ψ_1 is the linear phase shift between intensity and frequency. Equations (2–4) can now be combined as follows:

$$I_t(t) = [\bar{I}_0 + i_0\cos(2\pi f t + \psi_1)]\exp[-\alpha(\bar{\nu} + a\cos(2\pi f t))] \tag{5}$$

Recognizing that the function is even and can be expanded using the Fourier cosine series, we obtain

$$\exp[-\alpha(\bar{\nu} + a\cos(2\pi f t))] = \sum_{k=0}^{\infty} H_k(\bar{\nu}, a)\cos(2\pi k t) \tag{6}$$

$$H_0(\bar{\nu}, a) = \frac{1}{2\pi}\int_{-\pi}^{\pi}\exp[-\alpha(\bar{\nu} + a\cos(\xi))]\,\mathrm{d}\xi \tag{7}$$

$$H_k(\bar{\nu}, a) = \frac{1}{\pi}\int_{-\pi}^{\pi}\exp[-\alpha(\bar{\nu} + a\cos(\xi))]\cos(k\xi)\,\mathrm{d}\xi \tag{8}$$

$$\alpha_\nu = \int_0^L S(x)\cdot P(x)\cdot\chi(x)\cdot\phi(x)\,\mathrm{d}x \tag{9}$$

Note that in Eqs. (7) and (8), the integration variable is designated as ξ instead of θ as in [8–11]. This is due to the fact that θ appears in later equations as the crossing half-angle used in crossed-beam Doppler shift velocimetry. In Eq. (9) the absorbance has been expressed as the integral of the product of linestrength S (cm^{-2} atm^{-1}), pressure P (atm), mole fraction of the absorbing species, χ, and lineshape function ϕ_ν, with each parameter being allowed to vary with x, the position along the line of sight. In the case of a uniform line of sight, the absorbance in Eq. (9) reduces to $k_\nu L$, and the previous equations are identical to those in [3,6–8].

The transmitted intensity then passes through a lock-in amplifier, which consists of a mixer and a low-pass filter, producing an X and Y component at the output:

$$X_{2f} = \frac{G\bar{I}_0}{2}\left[H_2 + \frac{i_0}{2}(H_1 + H_3)\cos\psi_1\right] \tag{10}$$

$$Y_{2f} = -\frac{G\bar{I}_0}{2}\left[\frac{i_0}{2}(H_1 - H_3)\sin\psi_1\right] \tag{11}$$

Here, G, the detector gain, now appears in these equations. The $2f$ signal is given by the root sum square of the two components:

$$S_{2f} = \sqrt{X_{2f}^2 + Y_{2f}^2} \qquad (12)$$

As described in [8,9,11–13], normalization with the $1f$ signal is used to remove the dependence of the $2f$ signal on detector gain and average laser power. Similar equations for the $1f$ signal are produced:

$$X_{1f} = \frac{G\bar{I}_0}{2}\left[H_1 + i_0\left(H_0 + \frac{H_2}{2}\right)\cos\psi_1\right] \qquad (13)$$

$$Y_{1f} = -\frac{G\bar{I}_0}{2}\left[i_0\left(H_0 - \frac{H_2}{2}\right)\sin\psi_1\right] \qquad (14)$$

$$R_{1f} = \sqrt{X_{1f}^2 + Y_{1f}^2} \qquad (15)$$

Equations (7–15) provide the basis for simulating the path-integrated WMS-$2f/1f$ lineshape along a nonuniform line of sight. Note that Eqs. (10–15) are the same as those applied to cases with a uniform line of sight; only the formulation of the absorbance in Eq. (9) is affected by nonuniformities in the beam path. The overall nonuniform lineshape includes the effects of different pressures, mole fractions, and temperatures (through the linestrength and lineshape functions) experienced at each point along the line of sight. The analysis will now proceed to consider the effects of Doppler-shifting of the lineshape caused by flow velocity.

A typical setup for TDLAS velocimetry is shown in Fig. 1. One beam is directed upstream in the flow while the second is directed downstream. The detected lineshapes on either beam will experience frequency shifts of opposite sign, and the axial velocity, U, can be extracted by measuring the relative shift between the two lineshapes:

$$\Delta\nu/\nu_o = 2\sin\theta \cdot U/c \qquad (16)$$

Here, $\Delta\nu$ is the frequency shift (cm^{-1}), ν_o is the unshifted linecenter frequency (cm^{-1}), θ is the crossing half-angle seen in Fig. 1, and c is the speed of light (m/s). From Eq. (16) it can be seen that lineshapes along the beam path may experience slightly different frequency shifts caused by nonuniformity in the axial velocity, U, along the line of sight. To properly simulate the effects of velocity nonuniformity, Eqs. (7) and (8) are modified as follows:

$$H_0(\bar{\nu}, a) = \frac{1}{2\pi}\int_{-\pi}^{\pi} \exp[-\alpha(\bar{\nu} + \Delta\nu(x)/2 + a\cos(\xi))]\,d\xi \qquad (17)$$

$$H_k(\bar{\nu}, a) = \frac{1}{\pi}\int_{-\pi}^{\pi} \exp[-\alpha(\bar{\nu} + \Delta\nu(x)/2 + a\cos(\xi))]\cos(k\xi)\,d\xi \qquad (18)$$

The relative frequency shift $\Delta\nu$ [as defined in Eq. (16)], has now been included to indicate that the absorbance may be frequency-shifted due to velocity along the beam path (relative frequency shift is divided by two, since these equations consider absorption on a single beam). The sign of $\Delta\nu$ is positive for a beam directed downstream and negative for a beam directed upstream; the frequency shift is again a function of x, indicating that different velocities at points along the beam path will cause different magnitudes of frequency shift. Equations (9–18) now completely define the path-integrated WMS-$2f/1f$ lineshape allowing for temperature, pressure, mole fraction, and velocity nonuniformities along the laser line of sight. As described in the next section, these equations will be used to simulate WMS lineshapes in a nonuniform flow.

B. Lineshape Modeling

A CFD solution for the flow through the DCSCTF isolator where the mass-flux sensor was deployed was used to simulate lineshapes for lines of sight through nonuniform flow. The solution provides temperature, pressure, density, and uvw velocities in three dimensions. Hence this data can be compared with spatially resolved measurements taken by translating the TDLAS LOS during a run. Figure 2a shows the sensor mounted to stages to translate the sensor LOS. The setup can be configured to translate either vertically or horizontally across the duct.

In the vertical translation configuration of Fig. 2b, the lasers cross in a horizontal x-z plane, which was then translated vertically (y axis) across the duct. Similarly for the horizontal translation configuration of Fig. 2c, the lasers cross in a vertical x-y plane and were translated horizontally (z axis) across the duct. Because the sensor collects measurements as it translates across the duct, planes of CFD data (outlined in black) encompassing all laser lines of sight (indicated by the dashed arrows of Figs. 2b and 2c) can be evaluated. Spatial resolution was limited by the finite beam size of the laser; hence the CFD data, which was produced on a very fine spatial grid, was averaged over the beam diameter (approximately 1 mm). The CFD solution for pressure along the laser LOS for the vertical translation configuration is displayed in Fig. 3a. The planes of data for
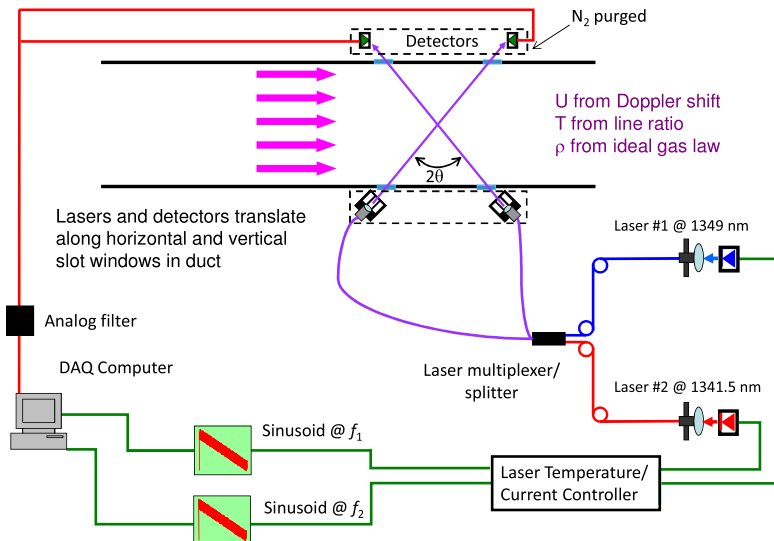
Fig. 1 **Two-laser frequency-multiplexed WMS sensor for mass flux at H_2O wavelengths λ_1 and λ_2 (~1349 and 1341.5 nm, respectively). Light from the two lasers is combined into a single fiber and then split to be directed upstream and downstream in the supersonic flow with a crossing angle 2θ. Velocity is determined from the relative Doppler shifts of the absorption lineshape, and gas temperature is determined from the ratio of the two absorption signals.**
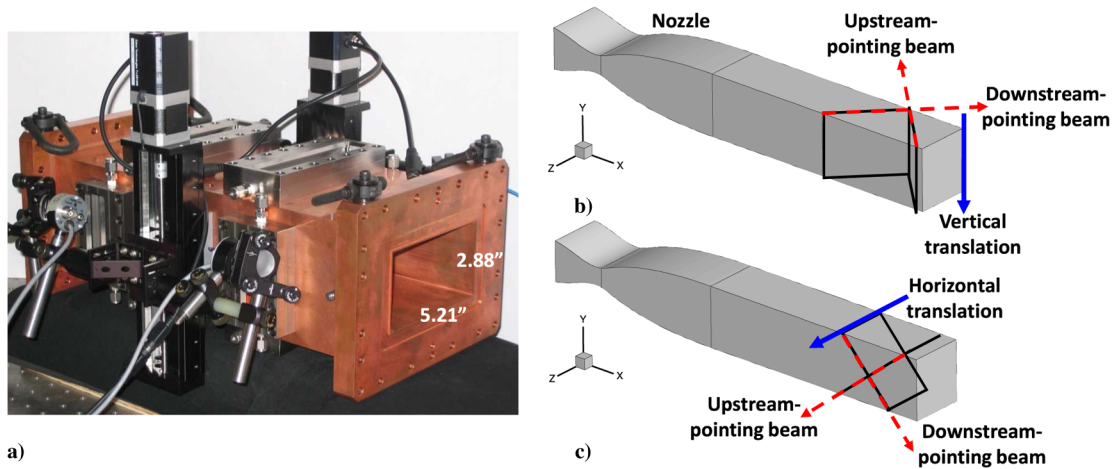
a)

b)

c)

Fig. 2 NASA DCSCTF isolator: a) section with TDLAS mass-flux sensor configured for vertical scanning, b) CFD geometry (symmetry about vertical axis is assumed) with vertical translation configuration shown, and c) CFD geometry with horizontal translation configuration shown.
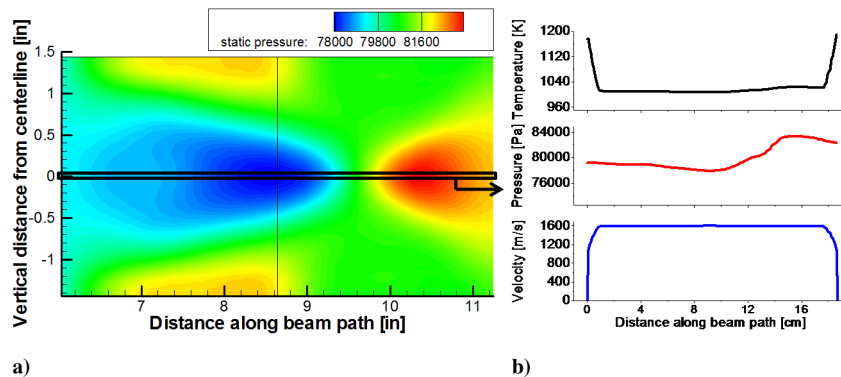

a)

b)

Fig. 3 Plots of a) CFD pressure data along laser LOS in vertical translation configuration (units are pascals) and b) temperature, pressure, and velocity data along LOS at the vertical center of duct.

temperature, velocity, and pressure were extracted along the diagonal laser path indicated by the red arrows shown in Fig. 2b.

The thin black box in Fig. 3a outlines the 1 mm region of the slice that was used to determine the CFD predicted conditions along the laser LOS in Fig. 3b. The variation of temperature, pressure, and axial velocity is plotted as a function of distance along the downstream-pointing beam for the sensor in the vertical translation configuration. These data were used with Eqs. (9–18) to compute the path-integrated lineshape for each LOS. The process was repeated at various vertical positions in order to compare with measurements taken using the TDLAS sensor. The path-integrated WMS lineshapes of Fig. 4 were calculated from the CFD data of Fig. 3b. The 1341 nm transition ($E'' = 1962.51$ cm^{-1}) with a modulation index $m = 0.9$ is considered in this analysis. In the vertical translation configuration, the path-integrated absorbance is roughly 0.16. A significant frequency shift (Doppler shift) can be seen between the lineshapes produced on the downstream- and upstream-pointing beams (illustrated in Figs. 2b and 2c). Note that the entire lineshape is positive, since the signal is the root sum square of the lock-in amplifier output [see Eqs. (12) and (15)].

The frequency shift can be measured at various points along the lineshape; however, to develop a high-speed, robust velocity detection algorithm, only the data in the laser frequency scan from the central peak to the two adjacent valleys is considered. Ideally, the velocities measured on either the high- or low-frequency face of the lineshape would be identical. However, the presence of nonuniformities in the beam path can distort the lineshape, causing slight differences in these measured frequency shifts.

Figure 5a shows the variation of velocity inferred from path-integrated lineshapes as a function of boundary-layer (BL) thickness, where the thickness of the boundary layer was defined as the distance

to the point at which the velocity reached 99% of the freestream value. In this analysis the same pressure, temperature, and mole fraction gradients were used for all boundary-layer thicknesses. We will first consider the top two curves in Fig. 5a (BL = 0.9 cm thick), which are produced with the data in Fig. 3b. It is clear that the simulated path-integrated velocity measurement is lower than the core velocity shown in the lower plot of Fig. 3b (1600 m/s). This is to be expected, since the measurement is obtained from a path-integrated lineshape, produced as the laser beam travels through two low-velocity boundary layers and the core flow. Indeed, when the previously described measurement technique was applied to lineshapes simulated with no boundary layers, the core velocity was recovered at all measurement points along the lineshape. Intuitively,
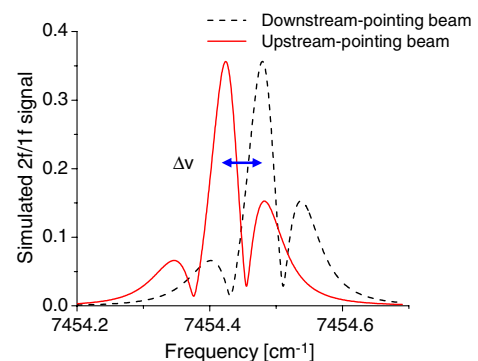

Fig. 4 Frequency-shifted path-integrated WMS-2f/1f lineshapes simulated from CFD data. Frequency shift corresponds to a 1600 m/s core flow.
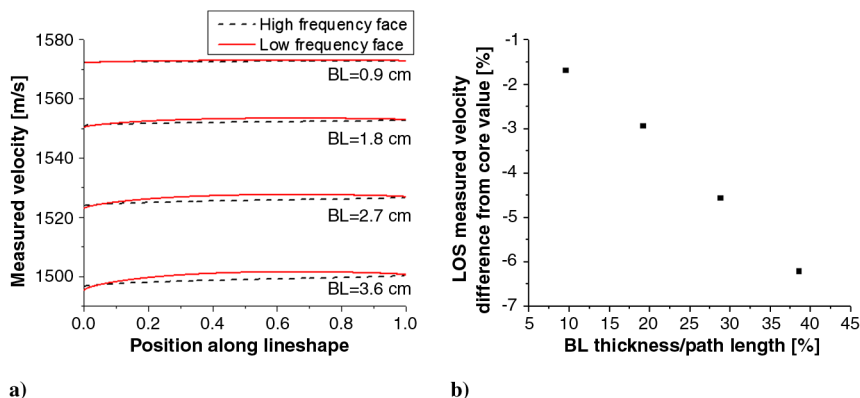
Fig. 5 Plots of a) measured velocities from path-integrated lineshapes with varying boundary-layer thickness (the position along lineshape refers to the location on the lineshape used for Doppler shift measurement, with 0 corresponding to the valley and 1 corresponding to the central peak) and b) mean difference between measured velocity of Fig. 5a and core velocity versus combined boundary-layer thickness as percentage of an 18.7 cm path length.

this suggests that the velocity inferred from LOS measurements should decrease as boundary-layer thickness increases, as illustrated in Fig. 5b.

It should be noted that in addition to an overall decrease in measured velocity as the boundary-layer thickness increases, the difference in velocity measured at various points along the lineshape also increases (moving along abscissa of Fig. 5a). This is due to increased distortion in the lineshape as the low-velocity boundary layers become a greater percentage of the path length. This distortion also contributes to the increasing discrepancy between velocities measured on the high- and low-frequency faces as boundary-layer thickness increases.

Figure 5b shows the mean deviation of the path-integrated measurement from the core velocity as a function of the combined boundary-layer thickness. The abscissa of Fig. 5b is computed as the percentage of the beam path along the 18.7 cm laser LOS that passes through the combined boundary layers. In the extreme case where roughly 40% of the laser LOS is contained in the boundary layers, only a 6% decrease in the path-integrated velocity measurement is expected. For the DCSCTF isolator, the CFD solution predicts that 10% of the path length is contained in the boundary layers, and a decrease of less than 2% in the path-integrated velocity measurement is expected. It is clear that for the current transition and modulation index, the sensitivity of the TDLAS measurement to nonuniformities is quite low. Optimal line selection and optimal choice of modulation index can minimize the TDLAS sensitivity to nonuniformities; however, this discussion lies beyond the scope of the current paper.

It is also seen that the decrease in the path-integrated velocity measurement is roughly linear with the boundary-layer thickness. This indicates that the path-integrated velocity measurement can be corrected in order to recover the core velocity. For example, with 10% of the beam path passing through boundary layers, the simulated path-integrated velocity measurement is roughly 1.5% lower than the core value, and the TDLAS measurement can be adjusted accordingly. In the next section, this analysis of spatially resolved lineshapes simulated with the CFD solution is used to correct velocity measurements in the NASA Langley DCSCTF to within 0.25% of the facility predicted value for the direct-coupled flow.

III. Measurements in NASA Langley DCSCTF

The DCSCTF at NASA Langley produces high-enthalpy flows for the testing of scramjet combustor concepts. H_2–air combustion is used to heat the flow before expansion through a supersonic nozzle

[14,15]. During testing of the TDLAS mass-flux sensor, a Mach 2.65 nozzle was used to simulate Mach 6 and 7 flight enthalpies, producing the nominal test conditions summarized in Table 1. These conditions were computed using a 1-D thermodynamic equilibrium solver based on input mass fluxes to the combustor, nozzle areas, and heater pressures [16,17]. The solver outputs predicted conditions at the nozzle exit based on the facility operating conditions for each run (input mass fluxes, heat losses, etc.). The DCSCTF flow tunnel is shown in a photograph in Fig. 6 with the major components labeled.

The mass-flux sensor was mounted on a custom isolator section located between the nozzle and the fuel injectors in Fig. 6. Optical access via slot windows on the isolator section is shown in Fig. 7a. These windows cover 3-mm-wide slots cut in the wall of the section to provide a crossing angle $2\theta = 90°$, as illustrated by the arrows in Fig. 7a.

All windows were 0.25-in.-thick BK-7 optical glass; window thickness was chosen such that internal reflections of the laser beam within the window would not be transmitted through the slots. The volume between the window and the slots was purged with heated nitrogen to minimize water vapor in the stagnant gases in the optical path through the isolator wall. The sensor optical components were attached to translation stages, as shown in Fig. 7b. The short optical paths external to the isolator were also purged with unheated nitrogen. The optical setup was translated on the vertical walls, then on the horizontal walls to enable measurements in both vertical and horizontal planes.

A. Velocity Measured in the DCSCTF

Figure 8a shows the time-resolved (50 Hz) velocity measured in the center of the channel with the sensor configured to probe the horizontal plane and a modulation index $m = 0.9$. After the initial startup transient of the tunnel (caused by a surge of flow after the hydrogen and oxygen supply valves fully open), the sensor measurement was in excellent agreement with the velocity computed from the facility predictive code mentioned earlier. The first plateau in velocity from 2.5 to 5 s corresponds to an H_2 and O_2 mass-flow rate of roughly 80% of the operating condition. The CFD solution for the isolator at the Mach 7 condition predicted the boundary-layer thickness to be roughly 7 mm. The uncorrected velocity measurements shown in Fig. 8a are roughly 1.7% lower than the facility predicted value; Fig. 8b shows the data of Fig. 8a with the boundary-layer correction and the improvement in agreement between measured and facility predicted velocities.

Table 1 Conditions for Mach 6 and 7 set points at NASA Langley DCSCTF

Flight enthalpy	Static pressure, kPa	Static temperature, K	Water mole fraction	Nozzle exit velocity, m/s
Mach 6	72	714	0.19	1440
Mach 7	72	935	0.25	1630

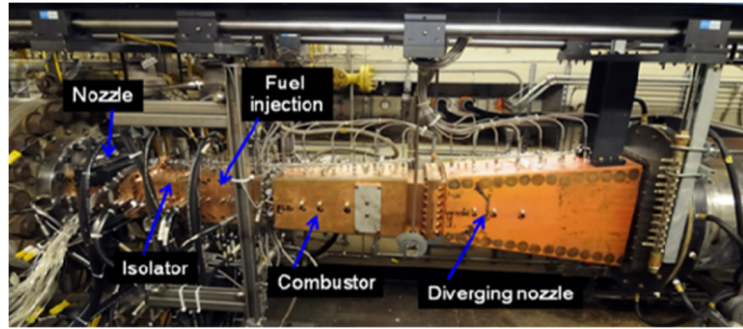Fig. 6   Photograph of the DCSCTF at NASA Langley showing flowpath sections as labeled.

a)   b)
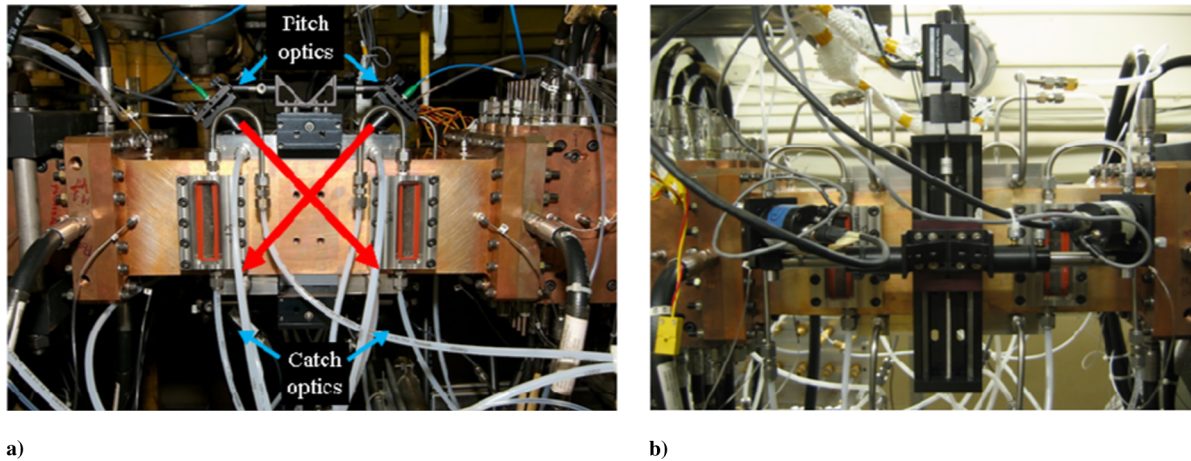
Fig. 7   Mass-flux sensor installed on custom isolator section: a) sensor configured to probe vertical planes of the flowpath; arrows illustrate the beam paths and b) sensor configured to probe horizontal planes of the flowpath.

By correcting for the presence of boundary layers, the difference between the sensor-measured velocity and the predicted velocity is reduced by more than a factor of 6, bringing the agreement to within 0.25% in a 1630 m/s flow. Because of the necessity for accurate measurement of mass flux, this improvement in accuracy by accounting for nonuniformities along the LOS is quite significant. Measurements were also made with a modulation index $m = 2.2$ to investigate the improvement in the sensor performance from the optimization of the modulation index as described in [8]. The use of an optimal modulation index reduced the standard deviation of the velocity after the startup transient by a factor of 3 ($\sigma = 14$ m/s for $m = 0.9$ versus $\sigma = 47$ m/s for $m = 2.2$). These data show that the velocity stability of flow in the tunnel and the sensor precision are better than 1% of the total 1630 m/s velocity after the startup transient.

The sensor was then translated during a test across the channel for spatially resolved measurements; a scan of vertical planes from the left to the right sidewall of the channel (looking downstream) is shown in Fig. 9a and a scan of horizontal planes from top to bottom is shown in Fig. 9b. The sensor was first positioned within 0.5 mm of the wall at its starting position (top wall for vertical translation, left sidewall for horizontal translation) and measurements were taken at ten points as the sensor was translated across the full height or width of the channel during a single tunnel run. At each point in Fig. 9, the sensor measurements were averaged for 1 s, and the error bars shown are the $1 - \sigma$ standard deviations of these average values. The total time for translation and data acquisition was 13 s. The optical alignment was degraded near the walls of the channel, where vibrations can block the edge of the laser beam; this reduced the signal-to-noise ratio of the transmitted intensity and produced a

a)   b)
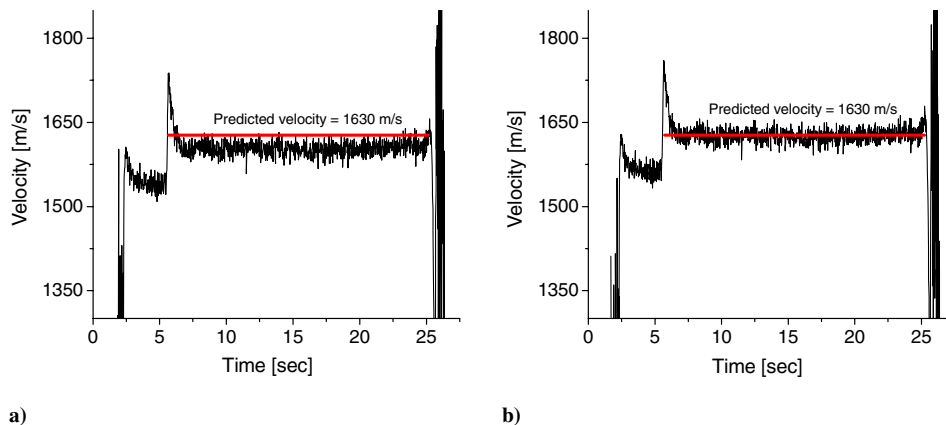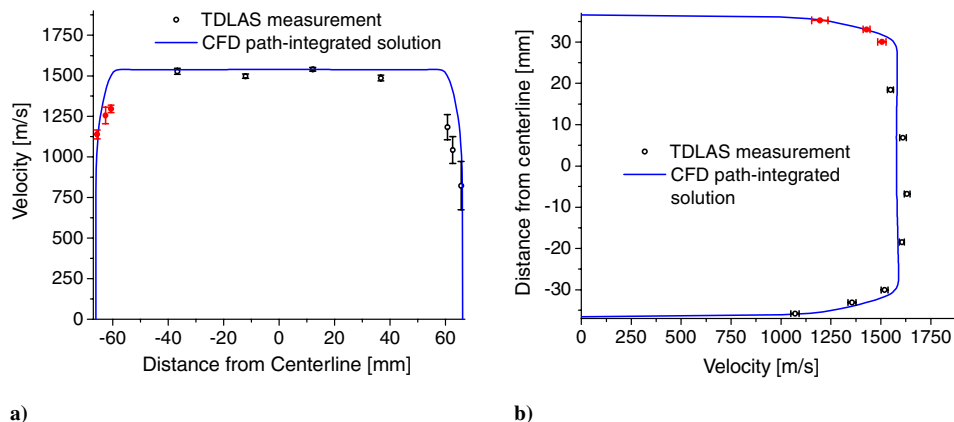
Fig. 8   Time-resolved velocity in the middle of the channel, horizontal plane: a) no correction and b) with correction for nonuniformity along LOS.

Fig. 9 Spatially resolved velocity (no correction applied) plotted from a) left to right of channel (facing downstream) in vertical planes and b) top to bottom of channel in horizontal planes. Solid data points indicate measurements taken during facility startup transient.

corresponding increase in the observed standard deviation shown in the error bars. The spatially resolved CFD velocity data were path-integrated along the sensor beam path, and the resulting values are plotted in Fig. 9 for comparison.

Overall there is good agreement between the CFD path-integrated solution and the measured values. The first three TDLAS measurements (solid data points in Figs. 9a and 9b) tend to be higher due to the startup transient seen in Fig. 8. In the vertical scan direction, the boundary-layer thickness predicted by the CFD ($\sim$9 mm) is confirmed by the TDLAS measurements. For the horizontal scan in Fig. 9a, the boundary-layer thickness may be underpredicted by the CFD simulation, although the TDLAS measurements agree closely in the core flow. These data demonstrate that the sensor has the capability to make precise, accurate, spatially resolved velocity measurements in the high-speed, high-temperature flow of the DCSCTF at NASA Langley.

B. Temperature Measured in the DCSCTF

Temperature was determined simultaneously with velocity during all runs. Both laser wavelengths were multiplexed onto the upstream and downstream beams, and temperature was determined by comparing the measured $1f$-normalized WMS-$2f$ peak values with simulations for both beam paths. The 1349 nm laser was modulated at $m = 2.2$ and the 1341 nm laser at $m = 0.9$ for velocimetry. As described in [8–11], the WMS-$2f$ signal is maximized at $m = 2.2$ and hence changes slowly in response to perturbations such as flow nonuniformity; while only the 1349 nm laser was modulated at $m = 2.2$, this mitigated the influence of nonuniformity on the temperature measurement. Time-resolved temperature data are plotted in Fig. 10 with the Mach 7 flight condition on the left and the Mach 6 flight condition on the right. These data were measured at the

center of the flow for a horizontal plane at Mach 7 and a vertical plane for Mach 6. The temperatures for the downstream- and upstream-pointing beams are in excellent agreement, as expected. The $1 - \sigma$ standard deviation of the average temperature after the startup transient is $\sim$10 K for both conditions. The gas temperature predicted by the facility model is also in excellent agreement with the measured data after the startup transient. More measurements are required to determine if the slow variation in gas temperature is a real facility effect or a measurement artifact, although the gradual rise in temperature during the run could reflect the change in wall losses as the test-section temperature increases. In Fig. 10b, the fluctuations in temperature are a result of the facility being unable to steadily maintain the Mach 6 flight condition (the nozzle used is designed for the Mach 7 condition).

C. Mass Flux Measured in the DCSCTF

The velocity and temperature data were combined with facility pressure measurements to determine the mass flux as the product of velocity and density. For these data the $\lambda_1 \sim 1349$ nm laser was modulated at $m = 2.2$ and $\lambda_2 \sim 1341$ nm was modulated at $m = 0.9$. The time-resolved mass flux is shown in Fig. 11, measured in the center horizontal plane for the Mach 7 flight condition in the left panel (Fig. 11a), and in the center vertical plane for the Mach 6 flight condition in the right panel (Fig. 11b). The data for mass flux from the downstream- and upstream-pointing beams are nearly identical, as expected from the excellent agreement in the temperature data from Fig. 10. There is also close agreement between the measured values and those predicted from the facility model; however, deviations occur near the beginning of the test due to the startup transient and toward the end of the test as the input gas mass flows decreased. The decrease in the measured mass flux was primarily caused by a
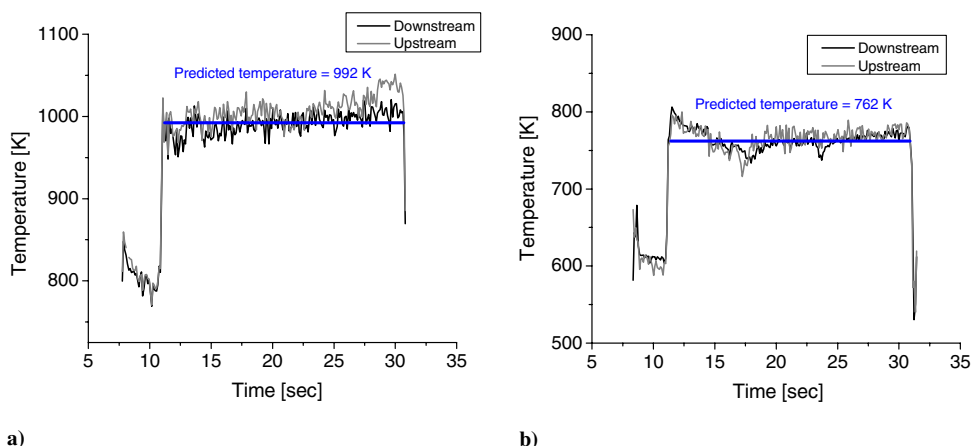
Fig. 10 Gas temperature for downstream- and upstream-pointing beams a) in the center horizontal plane for the Mach 7 flight condition and b) in the center vertical plane for the Mach 6 flight condition on the right. Facility model value also shown.
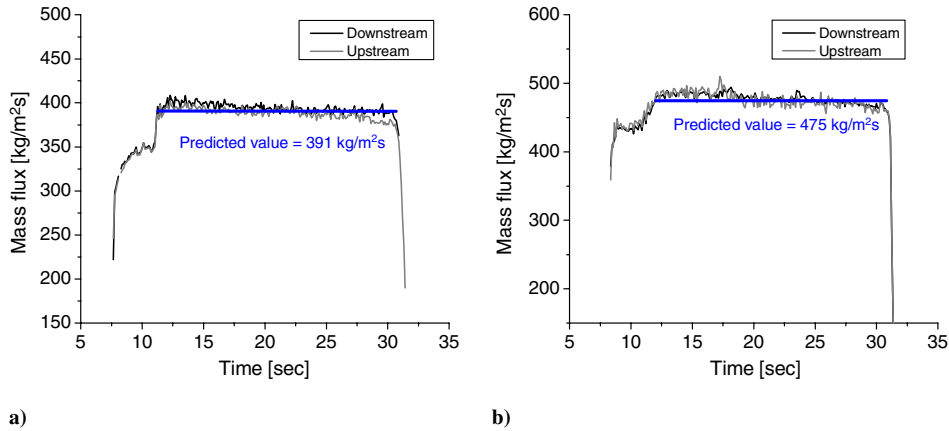
Fig. 11 Mass flux using temperatures taken with downstream- and upstream-pointing beams: a) in the center horizontal plane for the Mach 7 flight condition and b) in the center vertical plane for the Mach 6 flight condition. Facility model value also shown.
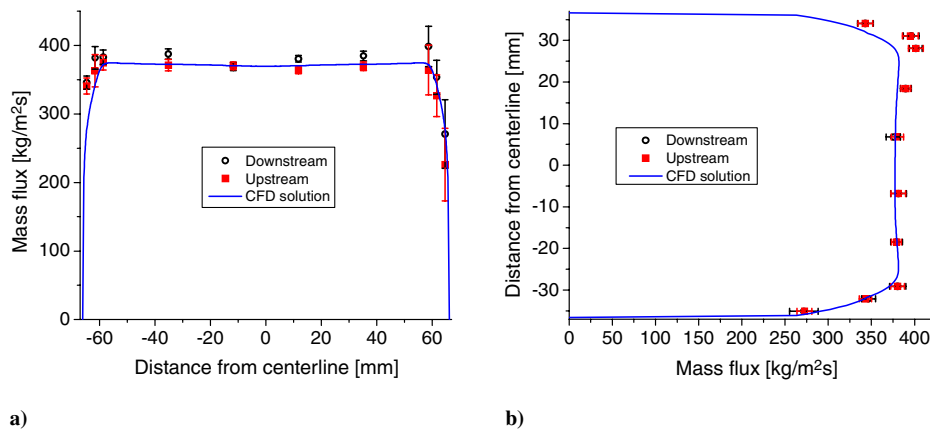

Fig. 12 Spatially resolved mass flux at Mach 7 condition plotted from a) left to right of channel (facing downstream) in vertical planes and b) top to bottom of channel in horizontal planes.

decrease in the O_2 mass-flow rate supplied to the facility. The TDLAS measurements confirm that the mass flux was nearly constant during a run and demonstrate the sensor's ability to detect slight deviations in mass flux caused by changes in the input mass-flow rates.

Temperature and velocity data collected at various points within the duct were processed to produce the spatially resolved mass-flux measurements in Fig. 12. The sensor measurements are in good agreement with the CFD solution; again, the three outliers at the far left of Fig. 12a and top of Fig. 12b are a result of increased mass flow during the startup transient. As mentioned previously, optical alignment tends to be poorer near the edges of the slot windows, resulting in the higher standard deviations seen in the sensor measurements near the walls. Overall, the sensor measurements show that there is good spatial uniformity within the test section and prove that the CFD solution correctly models the DCSCTF flow conditions.

IV. Conclusions

TDLAS of water vapor at 1.4 μm was demonstrated to provide accurate, spatially and temporally resolved mass-flux measurements in a high-speed, high-temperature flow in the DCSCTF at NASA Langley. An analysis of the effects of nonuniformity in temperature, pressure, mole fraction, and velocity on the WMS-$2f/1f$ lineshape was presented for the first time. By incorporating a CFD solution for the flow within the DCSCTF isolator section, path-integrated WMS-$2f/1f$ lineshapes were produced, accounting for nonuniform conditions along the laser LOS. A correction to recover the core velocity from the path-integrated velocity as a function of boundary-layer thickness was developed. The sensor was then deployed in the DCSCTF at NASA Langley in a custom isolator flow section with

optical access. Measurements of mass flux, temperature, and velocity were found to be in close agreement with both the facility predictive code (a 1-D thermodynamic equilibrium solver) and a CFD solution. The TDLAS velocity measurement was corrected using the CFD path-integrated simulations to within 0.25% of the value predicted by the facility code. Finally, spatially resolved mass-flux measurements were shown to be in good agreement with the CFD solution, demonstrating the sensor's capability to make accurate measurements with spatial resolution on the order of a beam diameter (1–2 mm). These results demonstrate the potential of TDLAS sensing for accurate mass-flux measurements in ground-test facilities and the potential for improving line-of-sight TDL measurements in nonuniform flowfields.

References

[1] Van Wie, D. M., and Laurel, M. D., "Techniques for the Measurement of Scramjet Inlet Performance at Hypersonic Speeds," AIAA 4th International Aerospace Planes Conference, AIAA Paper 1992-5104, Orlando, FL, Dec. 1992.

[2] Pellett, G. L., Bruno, C., and Chinitz, W., "Review of Air Vitiation

Effects on Scramjet Ignition and Flameholding Combustion Processes," 38th AIAA/ASME/SAE/ASEE Joint Propulsion Conference & Exhibit, AIAA Paper 2002-3880, Indianapolis, IN, Jun. 2002.

[3] Upschulte, B. L., Miller, M. F., and Allen, M. G., "Diode Laser Sensor for Gasdynamic Measurements in a Model Scramjet Combustor," *AIAA Journal*, Vol. 38, No. 7, 2000, pp. 1246–1252.
doi:10.2514/2.1094

[4] Philippe, L. C., and Hanson, R. K., "Laser Diode Wavelength-Modulation Spectroscopy for Simultaneous Measurement of Temperature, Pressure, and Velocity in Shock-Heated Oxygen Flows," *Applied Optics*, Vol. 32, No. 30, 1993, pp. 6090–6103.
doi:10.1364/AO.32.006090

[5] Hanson, R. K., "Spectroscopy-Based Thrust Sensor for High-Speed Gaseous Flows," U.S. Patent 5178002, 1993.

[6] Lyle, K., Jeffries, J. B., and Hanson, R. K., "Diode Laser Sensor for Air Mass Flux Based on Oxygen Absorption: II. Non-Uniform Flow Modeling and Aeroengine Tests," *AIAA Journal*, Vol. 45, No. 9, 2007, pp. 2213–2223.
doi:10.2514/1.27683

[7] Miller, M. F., Kessler, W. J., and Allen, M. G., "Diode Laser-Based Air Mass Flux Sensor for Subsonic Aeropropulsion Inlets," *Applied Optics*, Vol. 35, No. 24, 1996, pp. 4905–4912.
doi:10.1364/AO.35.004905

[8] Chang, L. S., Jeffries, J. B., and Hanson, R. K., "Mass Flux Sensing via Tunable Diode Laser Absorption of Water Vapor," *AIAA Journal*, Vol. 48, No. 11, 2010, pp. 2687–2693.
doi:10.2514/1.J050544

[9] Rieker, G. B., Jeffries, J. B., and Hanson, R. K., "Calibration-Free Wavelength-Modulation Spectroscopy for Measurements of Gas Temperature and Concentration in Harsh Environments," *Applied Optics*, Vol. 48, No. 29, 2009, pp. 5546–5560.
doi:10.1364/AO.48.005546

[10] Li, H., Farooq, A., Jeffries, J., and Hanson, R., "Near-Infrared Diode Laser Absorption Sensor for Rapid Measurements of Temperature and Water Vapor in a Shock Tube," *Applied Physics B (Lasers and Optics)*, Vol. 89, Nos. 2–3, 2007, pp. 407–416.
doi:10.1007/s00340-007-2781-9

[11] Li, H., Rieker, G. B., Liu, X., Jeffries, J. B., and Hanson, R. K., "Extension of Wavelength-Modulation Spectroscopy to Large Modulation Depth for Diode Laser Absorption Measurements in High-Pressure Gases," *Applied Optics*, Vol. 45, No. 5, 2006, pp. 1052–1061.
doi:10.1364/AO.45.001052

[12] Rieker, G. B., Li, H., Liu, X., Jeffries, J. B., Hanson, R. K., Allen, M. G. et al., "A Diode Laser Sensor for Rapid, Sensitive Measurements of Gas Temperature and Water Vapour Concentration at High Temperatures and Pressures," *Measurement Science and Technology*, Vol. 18, 2007, pp. 1195–1204.
doi:10.1088/0957-0233/18/5/005

[13] Farooq, A., Jeffries, J. B., and Hanson, R. K., "Sensitive Detection of Temperature Behind Reflected Shock Waves Using Wavelength Modulation Spectroscopy of CO2 Near 2.7 μm," *Applied Physics B (Lasers and Optics)*, Vol. 96, No. 1, 2009, pp. 161–173.
doi:10.1007/s00340-009-3446-7

[14] Guy, R. W., Rogers, R. C., Puster, R. L., Rock, K. E., and Diskin, G. S., "The NASA Langley Scramjet Test Complex," 32nd ASME, SAE, and ASEE, Joint Propulsion Conference and Exhibit, AIAA Paper 1996-3243, Lake Buena Vista, FL, Jul. 1996.

[15] Springer, R. R., Cutler, A. D., Diskin, G. S., and Smith, M. W., "Conventional/Laser Diagnostics to Assess Flow Quality in a Combustion-Heated Facility," 35th AIAA/ASME/SAW/ASEE Joint Propulsion Conference and Exhibit, AIAA Paper 99-2170, Los Angeles, Jun. 1999.

[16] Auslender, A. H., "An Application of Distortion Analysis to Scramjet-Combustor Performance Assessment," *1996 JANNAF Propulsion and Joint Subcommittee Meeting, Scramjet Performance Workshop*, Dec. 1996.

[17] Cutler, A. D., Danehy, P. M., Springer, R. R., O'Byrne, S., Capriotti, D. P., and DeLoach, R., "Coherent Anti-Stokes Raman Spectroscopic Thermometry in a Supersonic Combustor," *AIAA Journal*, Vol. 41, No. 12, 2003, pp. 2451–2459.
doi:10.2514/2.6844

R. Lucht
Associate Editor